Received: 7 June 2018 | Revised: 28 November 2018 | Accepted: 10 January 2019
DOI: 10.1111/jace.16325

ORIGINAL ARTICLE

Journal of the American Ceramic Society

Laser-quality Tm:$(Lu_{0.8}Sc_{0.2})_2O_3$ mixed sesquioxide ceramics shaped by gelcasting of well-dispersed nanopowders

Huajun Wu[1,2] | **Guo-Hui Pan**[1] | **Zhendong Hao**[1] | **Liangliang Zhang**[1] | **Xia Zhang**[1] | **Ligong Zhang**[1] | **Haifeng Zhao**[1] | **Jiahua Zhang**[1]

[1]State Key Laboratory of Luminescence and Applications, Changchun Institute of Optics, Fine Mechanics and Physics, Chinese Academy of Sciences, Changchun, China

[2]University of Chinese Academy of Sciences, Beijing, China

Correspondence
Guo-Hui Pan and Jiahua Zhang, State Key Laboratory of Luminescence and Applications, Changchun Institute of Optics, Fine Mechanics and Physics, Chinese Academy of Sciences, Changchun, China.
Emails: pangh@ciomp.ac.cn; zhangjh@ciomp.ac.cn

Funding information
National Key R&D Program of China, Grant/Award Number: 2017YFB0403104, 2016YFB0701003, 2016YFB0400605; NSF of China, Grant/Award Number: 51772286, 51402284, 11604330; NSF of Jilin province, Grant/Award Number: 20150520022JH, 20160520171JH; innovation program of CIOMP

Abstract

Tm^{3+}-doped mixed sesquioxide transparent ceramics are attractive candidates for the generation of robust ~2.1 μm lasers. In this paper, laser-quality Tm:$(Lu_{0.8}Sc_{0.2})_2O_3$ mixed sesquioxide ceramics were shaped for the first time by gelcasting of well-dispersed nanopowders, which were obtained using a modified coprecipitation method. The dispersibility of starting nanopowders was largely improved using alcohol-water solvent. The rheological properties of slurries were optimized for gelcasting. We also investigated the densification behavior of the gel-casted green compacts. In contrast to the dry-pressing route, it was found that gelcasting could yield more homogeneous and transparent ceramics. The optical in-line transmittance of the ceramic rod 12 mm in length was as high as 80.3% at 2090 nm. Upon pumping the ceramic rod by 796 nm diode laser, a 1.88 W CW laser at 2090 nm was acquired with a slope efficiency of 24.6% (with respect to the input pump power).

KEYWORDS
gelcasting, nanopowders, sesquioxides, transparent ceramics

1 | INTRODUCTION

There is an increasing interest in ~2 μm lasers due to numerous applications based on strong absorption of water in this very wavelength region, such as laser radar, medical surgery and atmospheric sensing.[1,2] Furthermore, ~2 μm lasers are applicable as pump sources for mid-infrared OPOs. Many of these applications demand for wavelengths above 2 μm or even above 2.1 μm, since the absorption of the common mid-IR OPO material ZGP is much weaker at such wavelengths.[3,4]

Thulium (Tm^{3+}) doped solid-state laser have excited a growing interest for generation of ~2 μm laser radiation, since they can be pumped at ~800 nm, at which wavelength high-performance laser diodes are commercially available.[5,6] Tm^{3+}-doped sesquioxides Re_2O_3 (Re=Lu, Sc, Y) offer excellent properties as gain media such as high thermal conductivities, low phonon energies, high absorption, and emission cross sections.[5,7,8] Furthermore, the Tm^{3+}-doped sesquioxides feature a strong Stark splitting of the ground state ($^3H_6$) (>800 cm^{-1}), leading to very broad emission and gain spectra extending up to ~2.1 μm.[9] Moreover, this feature can be enhanced in mixed sesquioxides exhibiting a disorder crystal structure. Using a 1 at% Tm:$LuScO_3$ sesquioxide crystal, a CW output power of 705 mW at ~2.1 μm with a slope efficiency of 55% was previously obtained.[10] A 155 nm-broad (1960-2115 nm) tuning range of the laser emission was also demonstrated.[10] However, it is difficult to produce mixed sesquioxide crystals by conventional single-crystal synthesis methods due to high melting point.[11] Tm^{3+}-doped mixed sesquioxide transparent ceramics are more attractive candidates for an easier and size-scalable production.[12,13]

Very recently, ~2 μm laser operation based on Tm^{3+}-doped mixed sesquioxide ceramics were reported.[9,14,15] Xu et al[14] reported the CW laser output of 2 at% Tm:$LuScO_3$ ceramics at 1982 nm and the output power was 211 mW with a slope efficiency of 8.2%. As reported by Zhou et al,[15] Tm:$LuYO_3$ ceramics were also fabricated and the maximum output power at 2050 nm was 1.55 W with a slope efficiency of 19.9%. In Jing's literature, a 4.76 at% Tm:$(Lu_{2/3}Sc_{1/3})_2O_3$ transparent ceramics generated 1 W output laser at 2100 nm with a slope efficiency of 24% with respect to absorbed pump power.[9] Note that these mixed sesquioxide ceramics were fabricated by solid-sate reaction. This traditional technique generally requires repeated mechanical mixing and grinding, leading to possible contaminations. Furthermore, it is difficult to control the morphology and particle size of the resulting powders.

In addition to solid-state method, wet-chemical techniques were widely used to prepare nanopowders as the starting materials of ceramics. Nanoscale powders were found to have huge potential because of their unique properties such as small size, large surface energy, and low melting point. Among the methods of preparing nanopowders, the co-precipitation route has proved to be the most convenient and cost effective technique.[16,17] However, the powders produced by this wet-chemical process usually include large (>100 μm) and hard agglomerates, and then attempts in fabricating laser-quality ceramics using such powders often resulted in large grains and numerous morphological defects in the obtained ceramics.[18,19]

The homogeneity of green compact is of great importance for sintering transparent ceramics. Shaping processes should be carefully controlled to improve the particle coordination. Several studies on Al_2O_3,[20] Y_2O_3,[18] YAG,[21] and Lu_2O_3[22] have shown that the resulting optical properties, especially transparency, could be improved by suitable powder compaction. In nanosized particles, the strong interaction forces between these particles promote agglomerations, which make it more difficult to get green compacts with high microstructural homogeneity. The key to successful sintering of nanopowders is, therefore, a technique that provides green compacts with a most homogeneous arrangement of particles on a micro scale. Dry pressing was mostly doped in the shaping process of sesquioxide ceramics, whereas gelcasting were rarely used.[23,24] For dry-pressing shaping the external force can never drive an individual particle in the body to shift into an optimum position between its neighbors, whereas gelcasting process provides the freedom for particles to find this position on their own.[20] In recent years, gelcasting process has made great progress to obtained high-quality ceramics.[25–27]

This paper demonstrated the feasibility of using coprecipitated nanopowders to fabricated laser-quality Tm:$(Lu_{0.8}Sc_{0.2})_2O_3$ mixed sesquioxide ceramics through gelcasting. Well-dispersed nanopowders were synthesized via coprecipitation method using alcohol-water solvent. Using the obtained nanopowders, more homogeneous green compacts were shaped by gelcasting. Finally, the optical properties and laser performance of the sintered ceramics were investigated.

2 | EXPERIMENTAL PROCEDURE

2.1 | Powder synthesis

High-purity Lu_2O_3, Sc_2O_3, Tm_2O_3, and nitric acid (HNO_3, guarantee grade) were used as raw materials. Analytical grade ammonium hydrogen carbonate (NH_4HCO_3) and ammonium hydroxide (NH_4OH) were mixed at the molar ratio of 3:1 as the precipitant. The precipitant solution was prepared by dissolving the precipitant into alcohol-water solvent and the volume ratios of alcohol to water was 1:2. $Zr(NO_3)_4{\cdot}5H_2O$ were used as sintering aid. First, $Lu(NO_3)_3$, $Sc(NO_3)_3$, and $Tm(NO_3)_3$ were prepared by dissolving coarse Lu_2O_3, Sc_2O_3, and Tm_2O_3 powders in the nitric acid, and were mixed together according to the stoichiometric rate of $(Tm_{0.02}Zr_{0.03}Lu_{0.75}Sc_{0.2})_2O_3$. Next, the mixed solution was dripped into the precipitant solution under mild string. After finishing the precipitation process, the solution was stirred continuously for another 60 minutes. Then, the precipitates were collected by centrifugation, washed four times with deionized water and twice with ethanol thoroughly, and then dried at 80°C for 24 hours in an oven. Finally, the loose precursors were calcined in air at 1200°C for 2 hours to obtain Tm:$(Lu_{0.8}Sc_{0.2})_2O_3$ nanopowders.

2.2 | Shaping process

The shaping of the green compact was performed by different process:

1. The nanopowders were uniaxially pressed into Φ 20 mm disks at 10 MPa followed by cold isostatic pressing (CIP) at 200 MPa.
2. The gelcasting procedure in this study was similar to that reported in the previous publication.[28] First, premixed solution was prepared by adding 10 wt% monomer (Methacrylamide, MAM), 1 wt% cross-linking agent (N,N′-methylenebisacrylamide, MBAM) and different amount of dispersant (Polyacrylic acid, PAA) to

the deionized water. The pH of the aqueous solution was adjusted to ~10 by adding ammonia water ($NH_3{\cdot}H_2O$). Second, slurries with different solid loading were prepared by ball milling with the obtained nanopowders and premixed solution for 2 hours. Third, the initiator (Ammonium persulfate, APS) was added into the slurries. After mixing and degassing, the suspensions were poured into nonporous molds and gelled in an oven at 60°C for 1 hour. After gelation and demolding, the green compacts were dried at room temperature, followed by extra drying at 120°C and subsequent heating at 800°C to burn out the organic compound.

Green compacts were sintered at 1750°C for 20 hours under vacuum and hot isostatically pressed (HIPed) at 1700°C in argon at 200 MPa for 2 hours. And then the sintered samples were annealed at 1450°C for 20 hours in the air. Finally, the samples were mechanically polished with a lapping machine using Al_2O_3 pastes of 32, 16, 8, and 4 μm in size, successively. Final polishing was carried out to obtain a mirror polishing using 150 nm diamond suspensions.

2.3 | Characterization

Crystalline phase was characterized by a X-ray powder diffraction (XRD, D8 FOCUS, Bruker, Germany) with CuKα radiation (λ = 1.54056 Å). Structural refinement was carried out by the Rietveld method using the FullProf program. The microstructural features of the precursors and nanopowders were observed by a scanning electron microscopy (SEM, Model S-4800, Hitachi, Japan), which was equipped with X-ray energy dispersive spectrometry (EDS). Thermal behavior of the precursor was studied by thermogravimetry analysis and differential scanning calorimetry analysis (TG-DCS, STA PT 1600, LINSEIS, Germany) from room temperature to 1200°C at a heating rate of 10°C/min in air. Zeta potential of the suspension with a solid loading of 0.05 wt% was measured using a Zetasizer (Nano-ZS, Malvern, UK) and the pH of the suspension was adjusted with hydrogen nitrate (HNO_3) solution and $NH_3{\cdot}H_2O$. The density was measured by the Archimedes method, using ethyl alcohol as the immersion medium. A stress-controlled rheometer (KINEXUS LAB$^+$, Malvern, UK) with a parallel plate (40 mm in diameter) was employed to study the rheological behavior of the slurry. The viscosities were measured with the continuous shear mode increasing from 0.1 to 100 s^{-1} at 25°C. The shrinkage behaviors of the green compact shaped by gelcasting as a function of temperature were measured by a thermal mechanical analyzer (L75/VS/2400, LINSEIS, Germany). The heating rate was 5°C/min, and the measurement range varied from 20 to 1800°C. All the ceramics in our experiment were mirror polished on both sides. Microstructures of the green compact and thermally etched ceramics were observed by SEM, as well as an optical microscopy (Model BX53, OLYMPUS, Japan). The real in-line transmittance (RIT) and absorption spectra of the polished samples were recorded by an UV/VIS/NIR spectrometer (UV-3600 PLUS, SHIMADZU, Japan). Near-infrared photoluminescence and laser spectra were measured by a fiber optics optical meter (NIR QUEST, Ocean Optics, China).

3 | RESULTS AND DISCUSSION

The XRD pattern of the precursors and calcined nanopowders are exhibited in Figure 1A. Tm_2O_3, Lu_2O_3, and Sc_2O_3 have the same crystalline phase and belong to the bixbyite type $[^{VI}A_2]$ $[^{IV}O_3]$, which is body-centered cubic and with space group of Ia-3. The as-synthesized $Tm{:}(Lu_{0.8}Sc_{0.2})_2O_3$ precursors were amorphous and they were converted into the crystalline phase after calcination. During calcination

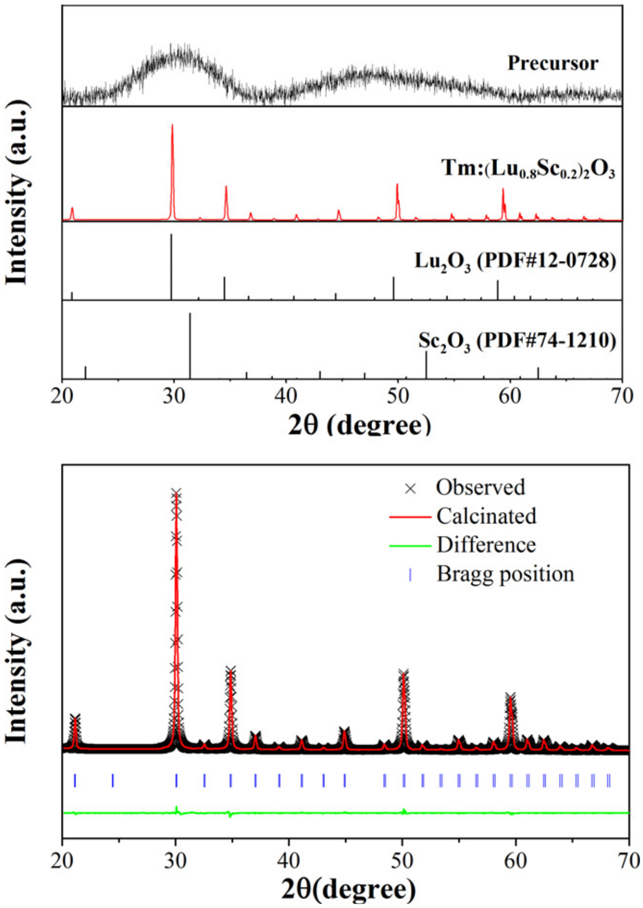

FIGURE 1 A, XRD pattern of the precursors and calcined nanopowders; B, Rietveld refinements of XRD data for 2at% Tm:$(Lu_{0.8}Sc_{0.2})_2O_3$ nanopowders. XRD, X-ray powder diffraction [Color figure can be viewed at wileyonlinelibrary.com]

process, the hydroxide or hydroxynitrate precursors were firstly decomposed into oxides with a weight loss of 30% (Figure S1), and then solid-state reactions would occur between the decomposed oxides to form single-phase solid solution. The solid solution has the same crystalline phase with Sc_2O_3 and Lu_2O_3. All the diffraction peaks were located between the diffraction patterns of Sc_2O_3 and Lu_2O_3, which could be confirmed by detailed XRD patterns in Figure S2. In order to further understand the microstructure of the calcined nanopowders, Rietveld structural refinements were performed using the previously reported crystallographic data of Lu_2O_3 as a starting mode. The observed, calculated and the different patterns of the XRD Refinement for 2at% $Tm:(Lu_{0.8}Sc_{0.2})_2O_3$ nanopowders are shown in Figure 1B. All the Rietveld R-factors, such as Rp (4.22), Rwp(4.57) and Chi2 (3.83) were acceptable, thus confirming the composition of the samples. EDS results (Figure S3) also confirmed the presence of Lu, Sc, and O elements in the powders and Tm element was not detected due to the lower content.

Figure 2 illustrates the micrographs of the precursors and the corresponding nanopowders. It can be observed from Figure 2A that the precursors presented big and compacted agglomerations 200-2000 nm in size when using distilled water as solvent. Those anomalous particles were the aggregation of primary nanowires. In comparison, spherical-shaped precursors were generated when using alcohol-water solvent. Those particle sizes ranged from 30 to 80 nm and only a few aggregations were observed. The above results indicated that the morphology of the obtained precursors could be well developed using alcohol-water solvent. The agglomeration is believed to be caused by the strong intra- and/or inter-molecular hydrogen bonding between hydroxide or hydroxynitrate precursors and water molecules.[29] The alcohol can play a role of disperser and contribute to the well-dispersed precursors. Generally speaking, hydrogen bonding interaction of alcohol is weaker than that of water, and alcohol was usually introduced as OH^- scavenging reagent. In our work, alcohol-water mixed solvent was employed to alleviate the agglomeration of the obtained precursors.

When the precursors in Figure 2A were calcined at 1200°C for 2 hours, the obtained powders were composed of hard agglomerates which could not be broken into monodispersed particles by ball milling. The agglomerate particles were determined to be 500 nm in agglomerate size, which was composed of primary particles (60 nm in size). This should be mainly ascribed to the corresponding precursors with heavy agglomeration. While the nanopowders synthesized with alcohol-water solvent were approximately uniform, spherical and well-dispersed. The mean particle size was ~90 nm, which was close to the estimated crystallite size by XRD analysis. Obviously, nanopowders with high dispersity were prone to homogenously compact to a high-density green compact. Higher transparency and uniformity is expected for the ceramics sintered from the powders without hard agglomerates.[30]

Gelcasting was chosen to obtain highly homogeneous green compacts. Generally, the key for successful gelcasting of ceramics is the obtaining of a fluid and stable slurry with a low viscosity and as high solids loading as possible. Figure 3 compares the zeta potential curves of the nanoparticles with and without 1.0 wt% PAA. Pure suspension in the absence of dispersant had an isoelectric point (IEP) near pH = 8.6. Whereas the IEP moved to pH = 4.4 in the presence of 1.0 wt% PAA. At pH = 10, the zeta potential

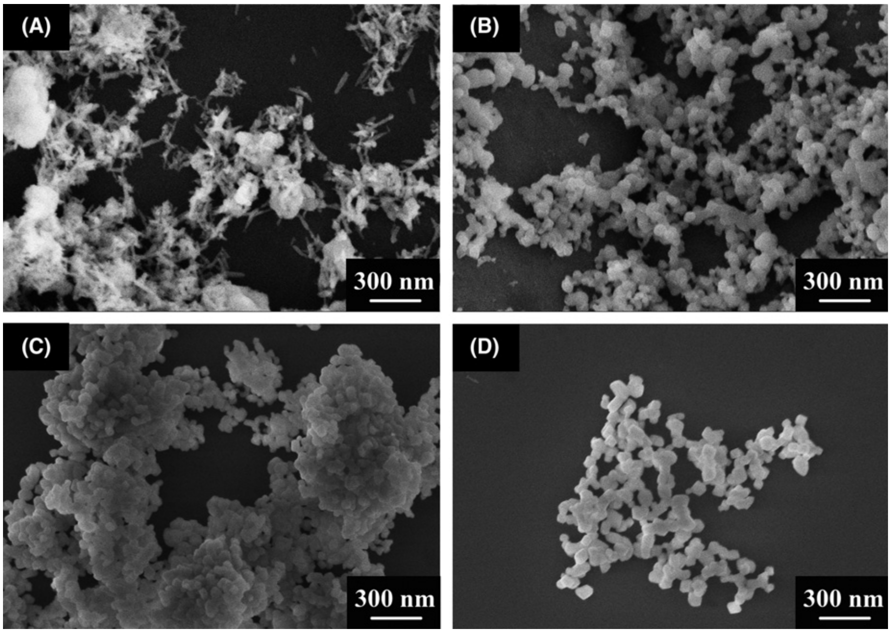

FIGURE 2 SEM imagines of the precursors synthesized with different solvent and the corresponding nanopowders after calcination (A) (C) using distilled water as solvent, (B) (D) using alcohol-water solvent

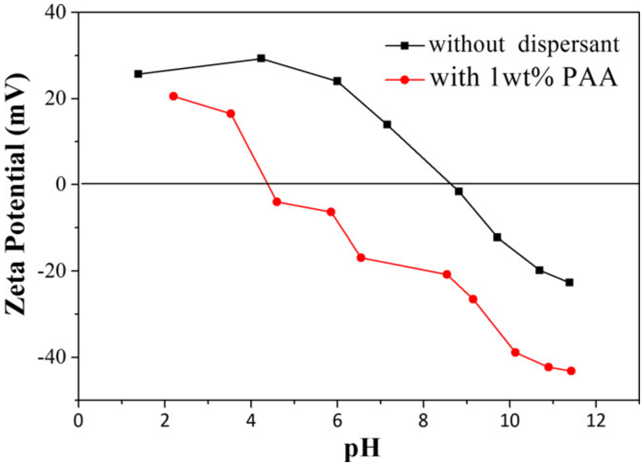

FIGURE 3 Zeta potentials of aqueous suspension as a function of PH with and without dispersant [Color figure can be viewed at wileyonlinelibrary.com]

decreased to −38 mV drastically, which further dropped but slightly as the pH was adjusted to above 10 by adding ammonia water. However, adding excess $NH_3 \cdot H_2O$ would release gaseous ammonia during gelation process, producing more bubbles. The effect of pH on viscosity of the slurry was also investigated (Figure 4). As the pH value of slurry increased from 8 to 10, the viscosity was significantly decreased from 0.7 to 0.07 Pa·s at the shear rate of 10 s^{-1}. The viscosity had an inverse association with the absolute Zeta potential. These results could be explained by the interaction between PAA and colloid nanoparticles. The acid-base dissociation constant (pKa) of the dispersant PAA is 4.3. In alkaline slurry, the PAA carboxyl (–COOH) pendant groups would be hydrolyzed into carboxylate (COO^-) ions according to the following reaction[31,32]:

$$RCOOH + NH_3 \rightarrow RCOO^- + NH_4^+ \quad (1)$$

The $RCOO^-$ species could be absorbed on the particle surface and contribute negative charges to the electrostatic double layer of the particles. As a consequence, the electrostatic repulsion forces among the particles were enhanced by the increase in the negative charges on the particle surface. The enhanced electrostatic repulsion forces would impede particle agglomeration and sedimentation, which is favorable to gelcasting process of slurry.

As shown in Figure S4, it is clear that all slurries exhibited a shear thinning behavior upon increasing shear rate. It is known that much liquid in the slurry was commonly immobilized in the inter-particulate gaps of the flocs and floc network of the slurry. When applying shear stress, the flocculated structure was broken down and the entrapped liquid was released, leading to slurry with low viscosity.[33]

Figure 5 shows the rheological curves of the slurry with 35 vol% solids loading versus dispersant content. All the slurries with 0.8-1.2 wt% PAA exhibited low viscosities, due to surface capping of particles by dispersants and increased dispersity. The viscosity decreased when increasing the PAA content from 0.8 to 1.0 wt%, but increased when adding more dispersants of 1.2 wt%. This was because excessive dispersant in the slurry would conjugate each other and formed polymer network; as a consequence, the viscosity increased.[34]

Slurry with high solid loading is necessary to improve the density of the green compact. However, higher solid loading often increases the slurry viscosity, which did not facilitate to cast the slurry into mold. The effect of solid loadings on the rhetorical behavior is shown in Figure 6. When the solid loading increased from 35 to 37 vol%, the viscosity apparently increased from 0.07 to 0.5 Pa·s at the shear rate of 10 s^{-1}. Slurry over 35 vol% was not suitable for casting, because its high viscosity could not fill the mold effectively. In addition, the bubbles in the viscous slurry could not be eliminated thoroughly, which was infaust to obtain homogeneous green compact. Based on

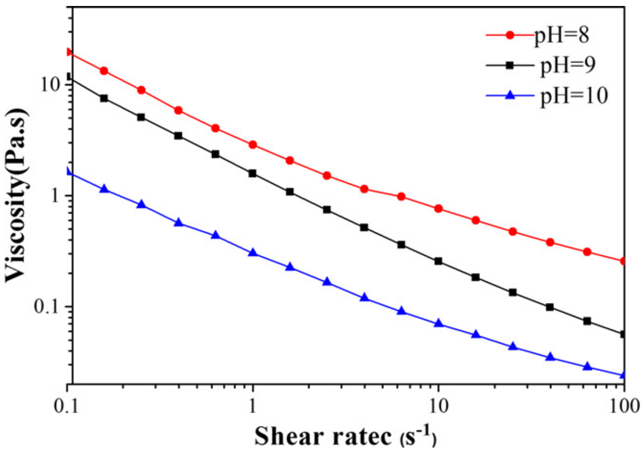

FIGURE 4 Effect of pH on viscosity of the slurries [Color figure can be viewed at wileyonlinelibrary.com]

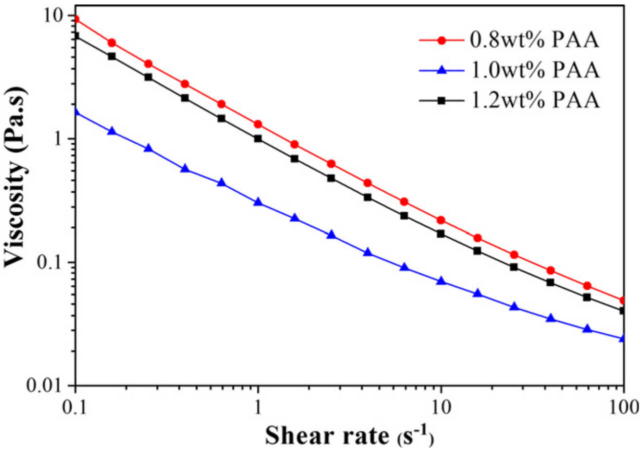

FIGURE 5 Viscosities of the slurries vs dispersant content [Color figure can be viewed at wileyonlinelibrary.com]

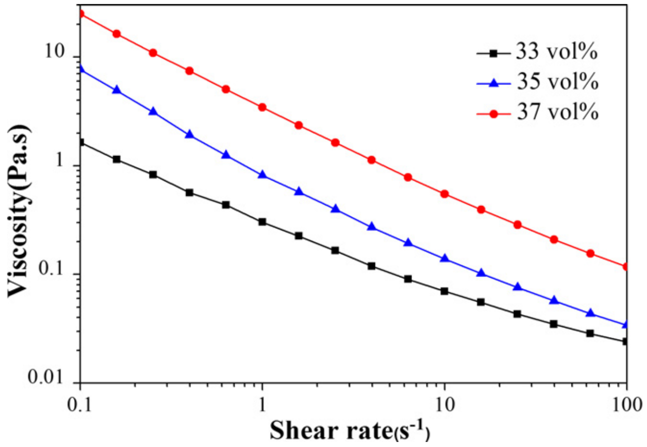

FIGURE 6 Viscosity of the slurries with different solid loadings [Color figure can be viewed at wileyonlinelibrary.com]

the obtained results, slurries with pH ~10, 35 vol% solid loading and 1.0 wt% PAA were prepared for gelcasting.

The inset of Figure 7 is the micrograph of the fracture surface of green compact obtained by gelcasting. The particles were almost uniform in size distribution and shape. No obvious defects or big pores were observed in the well packed green compact under this magnification level.

The densification is a process of pore elimination, and the pore elimination usually accompanies a compact shrinkage. Therefore, it should be possible to provide a clear demonstration on the densification behavior by examining the shrinkage curve of the green compact.[35] Figure 7 shows the linear shrinkage and linear shrinkage rate of gel-casted green compact. After burning out the organic compound, the as-obtained green compact displayed a uniform structure with relative density of about 55.2%. The onset of obvious shrinkage started at 800°C and the green compact reached a total shrinkage of 17.1% as the temperature ascended up to 1500°C. The relative density after sintering was about 99.1% without an isothermal hold. It is believed that the excellent densification performance of the Tm:$(Lu_{0.8}Sc_{0.2})_2O_3$ nanopowders compact originated from the more homogeneous green compact.[36,37]

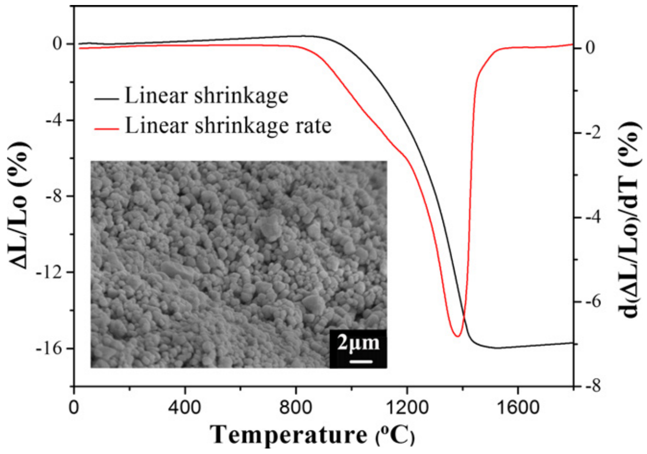

FIGURE 7 Shrinkage and shrinkage rate of gel-casted green compact and insert is the microstructure of green compact [Color figure can be viewed at wileyonlinelibrary.com]

For comparison, the green compacts were also shaped by dry pressing. Figure 8A,B represent the microstructures of the obtained ceramics observed by an optical microscope under transmission mode. For the dry-pressed sample, the microscope photograph was characterized by numerous splotches and white spots, caused by light reflection on scattering centers. SEM examination (Figure 8C) confirmed that these scattering centers were caused by the residual pores and abnormal grain growth. Regions of relatively small grains about 200-500 nm in size coexisted with some large grains about 1-3 μm in size. During the sintering process, some small grains did not grow significantly compared with the primary particle size (90 nm). Krell et al[20] demonstrated that the grain growth was slow during the intermediate stage (where most of the densification occurs) and the significant grain growth started at the transition from open to closed porosity. We speculated that the big pores and agglomerates formed during the shaping step would heterogenize the densification and open porosity remains at the final sintering stage, which would impede the grain growth. Such phenomena did not occur in the sample shaped by gelcasting. Only some small spots sporadically dispersed in the microstructure, indicated by larger red square (Figure 8B). There were almost no pores among or within the grains and the grain size was about 2-5 μm (Figure 8D). Notably, more homogeneous and uniform ceramics were obtained by gelcasting, because a more homogeneous green compact could be shaped by gelcasting.

Density of the samples shaped by dry pressing and gelcasting are shown in Table 1. Using the calculated lattice parameters, theoretical densities were estimated to be 8.3257 g/cm^3. Obviously, the green density of dry-pressed sample (after CIP) was much lower than that shaped by gel casting. That is due to the presence of large pores originated from agglomerates of individual particles. Through thermal process, most pores were eliminated and the relative density of both ceramics was higher than 99%. However, the mirror polished ceramics shaped by dry pressing was opaque because of the Rayleigh scattering by residual pores (porosity ~0.73%).

Figure 9 illustrates the optical transmittance of the mirror-polished 2 at% Tm:$(Lu_{0.8}Sc_{0.2})_2O_3$ ceramic(~12 mm in length) shaped by gelcasting. It could be seen that the transmittance at 2090 nm was as high as 80.8%, indicating the fabrication of excellent transparent ceramic. The theoretical transmittance was ~81.4% at 2090 nm, calculated from the formula:

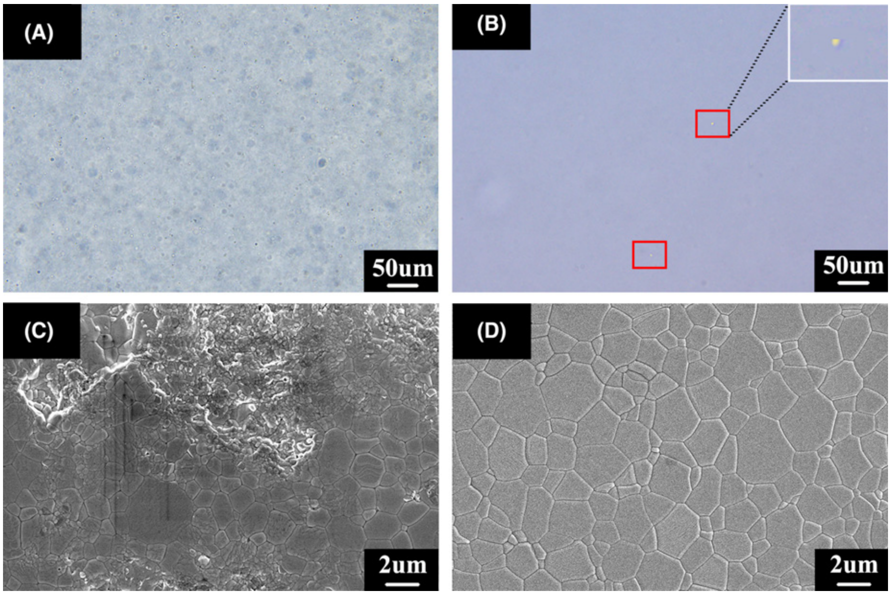

FIGURE 8 Optical transmission microscope photographs and the corresponding SEM image of the ceramics formed through different shape method (A) (C) dry pressing; (B) (D) gelcasting [Color figure can be viewed at wileyonlinelibrary.com]

TABLE 1 Density of the samples shaped by dry pressing and gel casting

	Green compacts		Ceramics	
	Density (g/cm^3)	**Relative density (%)**	**Density (g/cm^3)**	**Relative density (%)**
Dry pressing	3.8136	45.81	8.2647	99.27
Gelcasting	4.5958	52.20	8.3223	99.96

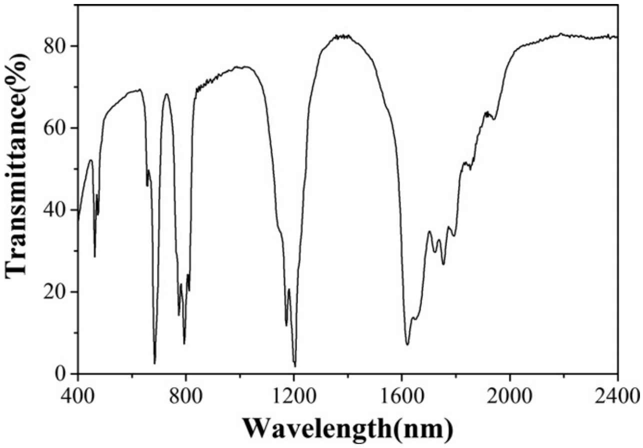

FIGURE 9 In-line transmittance of the gel-casted ceramic rod (12 mm in length)

$$T_o = \{1 - [(n-1)/(n+1)]^2\}^2 \tag{2}$$

where n and T_o represent the refraction index and theoretical transmittance of $Tm:(Lu_{0.8}Sc_{0.2})_2O_3$ ceramics, respectively.[38,39] RIT value obeys the Beer-Lambert law as follows:

$$T = T_o \exp(-\alpha x) \tag{3}$$

where T, α, and x denote RIT, attenuation coefficient and sample thickness, respectively.[22,38] Thus, the attenuation coefficient at the wavelength 2090 nm was ~0.006 cm^{-1}. Additionally, the RIT measured at 500 nm was 62.6%. The relative low transmittance at lower wavelength was caused by the residual nanometer pores (observed in Figure 8D), which activated higher Rayleigh scattering when light passed through the ceramic. Note that, according to Rayleigh's equation, the scatter intensity is proportional to λ^{-4} (λ is the wavelength) when the scatter center is smaller than the transmittance wavelength.[15]

Figure 10 displays the absorption and emission spectra of the ceramic at room temperature. The sharp absorption

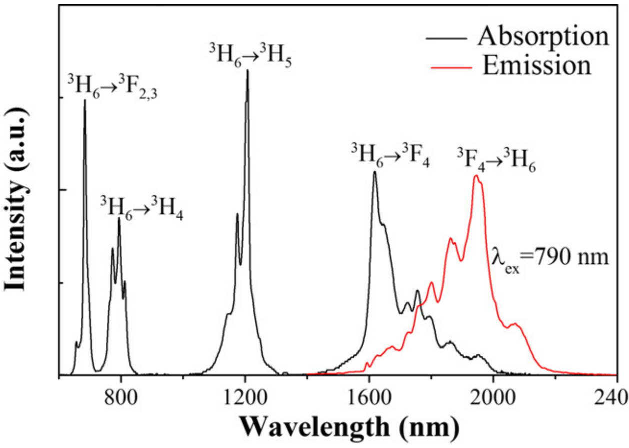

FIGURE 10 Absorption and emission spectra of $Tm:(Lu_{0.8}Sc_{0.2})_2O_3$ ceramics [Color figure can be viewed at wileyonlinelibrary.com]

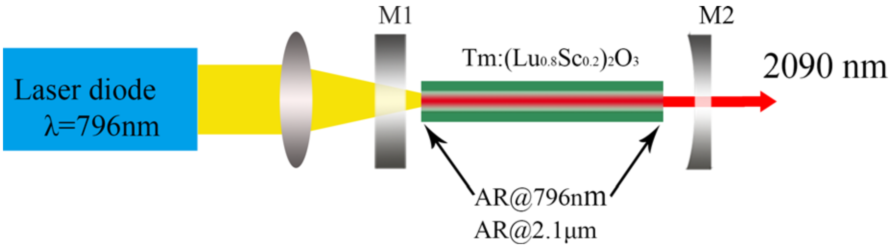

FIGURE 11 Experimental setup for CW Tm:$(Lu_{0.8}Sc_{0.2})_2O_3$ ceramic laser [Color figure can be viewed at wileyonlinelibrary.com]

bands centered at 686, 796, 1207, and 1625 nm were assigned to the transitions of Tm^{3+} ion from its ground state of $^3H_6$ to the excited states of $^3F_{2,3}$, $^3H_4$, $^3H_5$, and $^4F_4$, respectively.[6] A broad absorption spectrum extending from 760 to 820 nm with several pronounced peaks can be observed. The full width at half-maximum (FWHM) for the whole $^3H_6 \rightarrow {}^3H_4$ absorption band was ~38 nm, which was broader than that of Tm:Lu_2O_3 ceramic.[6] Its broad and efficient absorption at ~796 nm makes pumping possible with commercially available, powerful AlGaAs diode laser (LD), which granted a great advantage for the creation of effective 2.1 μm lasers.

For the laser experiment a simple and compact linear cavity setup was chosen and depicted in Figure 11. The laser gain media was a 2 at% Tm:$(Lu_{0.8}Sc_{0.2})_2O_3$ ceramic rod with a diameter of ~3 mm and a length of ~12 mm. Both facets of the rod had an antireflective (AR) coating for the pump and lasing wavelengths at 796 and 2090 nm, respectively. For better heat removal, the rod was wrapped in indium foil and mounted in a copper heatsink at constant temperature of ~20°C. The plane incoupling mirror M1 had high transmission at 796 nm and high reflection at 2090 nm. The curved output coupler M2 was partially transmitted (T_{oc} = 2.3%) at 2090 nm and highly reflective at 796 nm. The radius of curvature of M2 was 60 mm.

The laser oscillation from Tm:$(Lu_{0.8}Sc_{0.2})_2O_3$ sesquioxide ceramics shaped by gelcasting were investigated. A 796 nm commercial LD was used to pump the ceramic rod and continuous-wave (CW) laser output was measured, as shown in Figure 12. The threshold of absorbed pump power was 3.2 W and the maximum output power centered at 2090 nm reached 1.88 W with a slope efficiency of 24.6% (with respect to the input pump power). As compared with the previous reported mixed sesquioxide ceramics, the lasing performance in the present work was considerably improved.[9,14,15] However, the optical to optical efficiency was only 14.1%. We speculated the low conversion efficiency was mainly due to the scattering caused by trace amount of pores. The dependence of the lasing conditions such as T_{oc}, doping concentration of Tm, pump beam diameter as well as pump wavelength should be investigated. Our present experimental results indicated that laser-quality mixed sesquioxide ceramics could be shaped by gelcasting with the well-dispersed nanopowders and have great potential as gain media for high power ~2.1 μm laser.

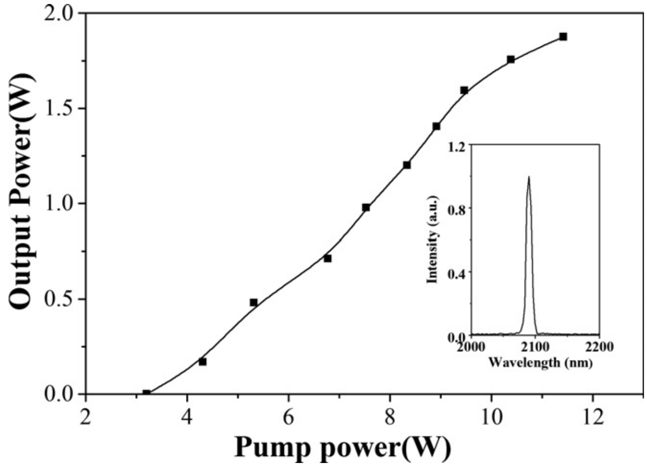

FIGURE 12 Input-output curve and the corresponding laser spectra (inset) of the CW ceramic laser

4 | CONCLUSION

We have demonstrated, for the first time, the laser oscillation from 2 at% Tm:$(Lu_{0.8}Sc_{0.2})_2O_3$ ceramics shaped by gelcasting of well-dispersed nanopowders, which were obtained by a modified co-precipitation method. Using alcohol-water solvent in the co-precipitated process, the dispersity of the nanopowders was improved markedly due to the weaker hydrogen bonding interaction. The slurry with 35 vol% solid loading, pH = 10 and 1.0 wt% PAA exhibited the optimum rheological property. More homogeneous and transparent ceramics were obtained by gelcasting than that shaped by dry pressing. The optical transmittance of the Tm:$(Lu_{0.8}Sc_{0.2})_2O_3$ ceramic with thickness of 12 mm was about 80.8% at 2090 nm. Moreover, when pumped with 796 nm LD, the maximum CW laser power at 2090 nm was 1.88 W with a slope efficiency of 24.6%.

ACKNOWLEDGMENTS

This work was supported by National Key R&D Program of China (Grant No. 2017YFB0403104, 2016YFB0701003, 2016YFB0400605), NSF of China (Grant No. 51772286, 51402284 and 11604330), NSF of Jilin province (Grant No. 20150520022JH and 20160520171JH), and innovation program of CIOMP.

ORCID

Huajun Wu https://orcid.org/0000-0002-5965-520X

REFERENCES

1. Scholle K, Lamrini S, Koopmann P, Fuhrberg P. 2 μm Laser sources and their possible applications. In: Pal B, editor. *Frontiers in guided wave optics and optoelectronics*. (InTech), 2010; pp. 471–500.
2. Kharitonov S, Bres CS. Isolator-free unidirectional thulium-doped fiber laser. Light-Sci Appl. 2015;4:e340.
3. Zawilski KT, Schunemann PG, Setzler SD, Pollak TM. Large aperture single crystal $ZnGeP_2$ for high-energy applications. J Cryst Growth. 2008;310(7):1891–96.
4. Koopmann P, Lamrini S, Scholle K, Schäfer M, Fuhrberg P, Huber G. Holmium-doped Lu_2O_3, Y_2O_3, and Sc_2O_3 for lasers above 2.1 μm. Opt Express. 2013; 21(3):3926–31.
5. Koopmann P, Lamrini S, Scholle K, Fuhrberg P, Petermann K, Huber G. Long wavelength laser operation of Tm:Sc_2O_3 at 2116 nm and beyond. In Conference "Advanced Solid-State Photonics 2011" (Istanbul, Turkey, 2011), paper $ATuA_5$.
6. Antipov OL, Novikov AA, Zakharov NG, Zinoviev AP. Optical properties and efficient laser oscillation at 2066 nm of novel Tm: Lu_2O_3 ceramics. Opt Mater Exp. 2012;2(2):183–89.
7. Takaichi K, Yagi H, Lu J, Bisson J-F, Shirakawa A, Ueda K, et al. Highly efficient continuous-wave operation at 1030 and 1075 nm wavelengths of LD-pumped Yb^{3+}:Y_2O_3 ceramic lasers. Appl Phys Lett. 2004;84(3):317–19.
8. Li J-G, Ikegami T, Mori T. Fabrication of transparent, sintered Sc_2O_3 ceramics. J Am Ceram Soc. 2005;88(4):817–21.
9. Jing W, Loiko P, Serres JM, Wang Y, Vilejshikova E, Aguiló M, et al. Synthesis, spectroscopy, and efficient laser operation of "mixed" esquioxide Tm:(Lu, Sc)$2O_3$ transparent ceramics. Opt Mater Exp. 2017;7(11):4192–202.
10. Koopmann P, Lamrini S, Scholle K, Fuhrberg P, Petermann K, Huber G. Laser operation and spectroscopic investigations of Tm: $LuScO_3$. In Conference "CLEO/Europe and EQEC 2011 Digest" *(Optical Society of America,2011), P. CA1_4.*
11. Lu J, Takaichi K, Uematsu T, Shirakawa A, Musha M, Ueda K, et al. Promising ceramic laser material: highly transparent Nd^{3+}: Lu_2O_3 ceramic. Appl Phys Lett. 2002;81(23):4324–26.
12. Koopmann P, Lamrini S, Scholle K, Fuhrberg P, Petermann K, Huber G. Efficient diode-pumped laser operation of Tm:Lu_2O_3 around 2 μm. Opt Lett. 2011;36(6):948–50.
13. Saarinen EJ, Vasileva E, Antipov O, Penttinen J-P, Tavast M, Leinonen T, et al. 2-mu m Tm:Lu_2O_3 ceramic disk laser intracavity-pumped by a semiconductor disk laser. Opt Express. 2013;21 (20):23844–50.
14. Xu X, Hu Z, Li D, Liu P, Zhang J, Xu B, et al. First laser oscillation of diode-pumped Tm^{3+}-doped $LuScO_3$ mixed sesquioxide ceramic. Opt Express. 2017;25(13):15322–29.
15. Zhou Z, Guan X, Huang X, Xu B, Xu H, Cai Z, et al. Tm^{3+}-doped $LuYO_3$ mixed sesquioxide ceramic laser: effective 2.05 um source operating in continuous-wave and passive Q-switching regimes. Opt Lett. 2017; 42(19):3781–84.
16. Li J-G, Ikegami T, Lee J-H, Mori T, Yajima Y. Co-precipitation synthesis and sintering of yttrium aluminum garnet (YAG) powders: the effect of precipitant. J Eur Ceram Soc. 2000;20(14–15):2395–405.
17. Wang NL, Zhang XY, Wang PH. Synthesis of Er^{3+}:Lu_2O_3 nanopowders by carbonate co-precipitation process and fabrication of transparent ceramics. J Alloy Compd. 2015;652:281–86.
18. Mouzon J, Lindbäck T, Odén M. Influence of agglomeration on the transparency of yttria ceramics. J Am Ceram Soc. 2008;91 (10):3380–87.
19. Gong H, Tang D-Y, Huang H, Ma J. Agglomeration control of Nd:YAG nanoparticles via freeze drying for transparent Nd:YAG ceramics. J Am Ceram Soc. 2009;92(4):812–17.
20. Krell A, Klimke J. Effects of the homogeneity of particle coordination on solid-state sintering of transparent alumina. J Am Ceram Soc. 2006;89(6):1985–92.
21. Esposito L, Piancastelli A, Costa AL, Serantoni M, Toci G, Vannini M. Experimental features affecting the transparency of YAG ceramics. Opt Mater. 2011;33(5):713–21.
22. Boulesteix R, Epherre R, Noyau S, Vandenhende M, Maître A, Sallé C, et al. Highly transparent Nd:Lu_2O_3 ceramics obtained by coupling slip-casting and spark plasma sintering. Scripta Mater. 2014;75:54–57.
23. Kijko VS, Maksimov RN, Shitov VA, Demakov SL, Yurovskikh AS. Sintering of transparent Yb-doped Lu_2O_3 ceramics using nanopowder produced by laser ablation method. J Alloy Compd. 2015;643:207–11.
24. Li X, Mao X, Feng M, Qi S, Jiang B, Zhang L. Fabrication of transparent La-doped Y_2O_3 ceramics using different La_2O_3 precursors. J Eur Ceram Soc. 2016;36:2549–53.
25. Olhero SM, Garcia-Gancedo L, Button TW, Alves FJ, Ferreira JMF. Innovative fabrication of PZT pillar arrays by a colloidal approach. J Eur Ceram Soc. 2012;32(5):1067–75.
26. Kaushal A, Olhero SM, Singh B, Bhardwaj C, Sharma I, Bdikin I, et al. 3D multiscale controlled micropatterning of lead-free piezoelectric electroceramics via Epoxy Gel Casting and lift-off. J Eur Ceram Soc. 2017;37(9):3079–87.
27. Sun Y, Shimai SZ, Peng X, Zhou GH, Kamiya H, Wang SW. Fabrication of transparent Y_2O_3 ceramics via aqueous gelcasting. Ceram Int. 2014;40(6):8841–45.
28. Wei N, Guan Y, Wu H, Lu Z, Chen X, Zhao Y, et al. Fabrication of Yb^{3+}-doped YAG transparent ceramics by aqueous gelcasting. J Sol-Gel Sci Technol. 2015;77(1):211–17.
29. Kim W, Baker C, Villalobos G, Frantz J, Shaw B, Sadowski B, et al. Highly transparent ceramics obtained from jet milled sesquioxide powders synthesized by co-precipitation method. Opt Mater Exp. 2014;4(12):2497–503.
30. Kim W, Baker C, Villalobos G, Frantz J, Shaw B, Lutz A, et al. Synthesis of high purity Yb^{3+}-doped Lu_2O_3 powder for high power solid-state lasers. J Am Ceram Soc. 2011;94(9):3001–05.
31. Wang K, Gan X, Li Z, Zhang D, Zhou K. Rheological properties of ITO slurries prepared from nano-powders for gelcasting process. Ceram Int. 2014;40(8):12623–28.
32. Appiagyei KA, Messing GL, Dumm JQ. Aqueous slip casting of transparent yttrium aluminum garnet (YAG) ceramics. Ceram Int. 2008;34(5):1309–13.
33. Li X, Li Q. YAG ceramic processed by slip casting via aqueous slurries. Ceram Int. 2008;34(2):397–401.
34. Shafeiey A, Enayati MH, Al-Haji A. The effect of slip casting parameters on the green density of $MgAl_2O_4$ spinel. Ceram Int. 2017;43(8):6069–74.

35. Liu DM, Tseng WJ. Influence of solids loading on the green microstructure and sintering behaviour of ceramic injection mouldings. J Mater Sci. 1997;32(24):6475–81.
36. Li J, Su X, Liu S, Li X, Li J-G, Huo D. A homogeneous co-precipitation method to synthesize highly sinterability YAG powders for transparent ceramics. Ceram Int. 2015;41(2):3283–87.
37. Trunec M, Maca K. Compaction and pressureless sintering of zirconia nanoparticles. J Am Ceram Soc. 2007;90(9):2735–40.
38. Kaminskii AA, Akchurin MS, Becker P, Ueda K, Bohatý L, Shirakawa A, et al. Mechanical and optical properties of Lu_2O_3 host-ceramics for Ln3 + lasants. Laser Phys Lett. 2008;5(4):300.
39. Medenbach O, Dettmar D, Shannon RD, Fischer RX, Yen WM. Refractive index and optical dispersion of rare earth oxides using a small-prism technique. J Opt A: Pure Appl Opt. 2001;3(3):174.

SUPPORTING INFORMATION

Additional supporting information may be found online in the Supporting Information section at the end of the article.

How to cite this article: Wu H, Pan G-H, Hao Z, et al. Laser-quality Tm:$(Lu_{0.8}Sc_{0.2})_2O_3$ mixed sesquioxide ceramics shaped by gelcasting of well-dispersed nanopowders. *J Am Ceram Soc*. 2019;102:4919–4928. https://doi.org/10.1111/jace.16325